2.1 Introduction

As discussed in the first chapter MOF requires two components to complete its framework-the organic linker and the metal ion node. MOFs of different topologies can be obtained by combining different SBU to coordinate with different linkers [1]. It has been observed that the term 'design' as a fascinating designation has been used for the synthesis of metal organic framework (MOF). The widespread acceptability of this phrase is still debatable, though numerous opposing reviews have come in for the term [2]. Before designing a novel MOF, several prerequisite knowledge should be acquired like the possible topologies of the SBUs, functionality of monodentate or multidentate organic linker, formation condition of metal ion coordinates etc. Also, the optimal conditions for the growth of crystallisation are necessary to achieve the intended phase for the framework [3]. The discovery of many MOFs is still in the exploratory stage as a result of this difficult asphalt in the production of MOF structures. Groundbreaking work on MOF synthesis has started among the groups of chemists studying coordination chemistry. At the same time people dealing with zeolite has started designing structures with organic molecules [4]. This explains why several synthesis methods, including electrochemical [5]–[7], mechanochemical [8],[9], solvothermal/hydrothermal [10]–[12], microwave-assisted [13],[14], steam-assisted, etc., are available for the production of MOFs.

In this work the synthesis of MOF (UiO-66) was carried out through a solvothermal route. The hydrothermal/solvothermal approach is a tedious procedure that typically needs a temperature that is higher than room temperature for the reaction to occur. In this method, the reaction is allowed to take place above the solvent's boiling point in closed containers under autogenous pressure. In the typical method metal salt and organic linker are mixed in a solvent where the precursors are soluble, allowed it to heat in a glass vial or Teflon lined autoclave depending upon the temperature it requires. In the ambient condition a precipitation reaction takes place followed by nucleation and crystal growth. The temperature plays a crucial role to achieve appropriate crystallinity and reaction rates which may impact the crystal morphology and lengthy response periods can potentially cause the MOF to degrade. In the reaction, when water replaces the solvent used, the route is termed as hydrothermal. This is a rather slow process in which the recrystallization may take place in more than two days. The system of interest in this case is Zr-based MOF

UiO-66 and its composites with other semiconducting materials, such as conducting polymers, metal oxides nanoparticles etc. The UiO-66 is one of the stable MOF known which makes it resistant to water, ethanol, benzene and other harsh chemicals. This is because of the strong SBU of UiO-66 which consists of six Zr cations which gives an overall octahedron topology. Each Zr in the SBU coordinates to carboxylate groups and oxo-hydroxy groups by bridging μ_3^-O and μ_3^-O to Zr ions. The great chemical and thermal stability of these MOFs can be attributed to zirconium's strong affinity for oxygen ligands and the compact structure of this SBU [15].

The materials considered for producing composites of UiO-66 were chosen in such a way that it can enhance the electrical transport properties alongside manifests a greater electrochemical activity. Therefore, Ag_2O NPs and PEDOT were incorporated into the framework of UiO-66 by post-synthetic modification methods. In this method the as prepared UiO-66 powder is treated with the precursors of Ag_2O NPs and PEDOT to give rise to the respective composites of Ag_2O@UiO-66 and PEDOT@UiO-66.

This chapter discusses the materials, methods, synthesis routes and fabrication of electrodes using MOFs and its composites. It also includes the basic principles of different experimental techniques and instrumentation employed for analysis of prepared samples. Different electrochemical techniques used to fulfil the application part are also highlighted in this chapter.

2.1.1   Physical properties of the materials

Table.2.1 Physical properties of precursors used for UiO-66 synthesis [16]

Precursors	Molecular Formula	Molecular weight (g/mol)	Melting Point (°C)	Boiling Point (°C)	Density (g/cm³)
Zirconium (IV) Chloride	$ZrCl_4$	233.04	437	331	2.80
1,4-benzene dicarboxylic acid (BDC)	$C_8H_6O_4$	166.13	300	Decomposes	1.519

Table.2.2 Physical properties of solvents used for synthesis [17]–[19]

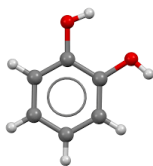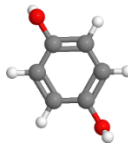| Solvent	Molecular Formula	Molecular weight (g/mol)	Melting Point (°C)	Boiling Point (°C)	Density (g/cm³)
n-dimethylformamide	$HCON(CH_3)_2$	73.09	-61	153	0.95
Methanol	CH_4O	32.04	-97.6	64.7	0.791
Ethanol	C_2H_6O	46.06	-114	78.37	0.789
Acetonitrile	CH_3CN	41.05	-44	81.25	0.787
Hydrochloric acid	HCl	36.5	-26 (38% solution)	48 (38% solution)	1.18

Table.2.3 Physical properties of the precursors used for incorporating guest into the framework [20],[21]

Precursors	Molecular Formula	Molecular weight (g/mol)	Melting Point (°C)	Boiling Point (°C)	Density (g/cm³)
EDOT	$C_6H_6O_2S$	142.18	10-11	193	1.331
Silver nitrate	$AgNO_3$	169.87	212	440	4.35

Table.2.4 Physical properties of reducing agent used [22]

Reducing Agent	Molecular Formula	Molecular weight (g/mol)	Melting Point (°C)	Boiling Point (°C)	Density (g/cm³)
Ferric chloride	$FeCl_3$	162.2	306	315	2.898
Sodium Hydroxide	$NaOH$	39.9	323	1,388	2.13

Table.2.5 Physical properties of the analytes used [23],[24]

Analyte	Molecular Formula	Molecular Weight(g/mol)	
Cadmium	Cd^{2+}	224.83	
Mercury	Hg^{2+}	200.59	
Catechol (CT)	$C_6H_6O_2$	110.1	
Hydroquinone (HQ)	$C_6H_6O_2$	110.11	

Biomolecules: Antibody mouse immunoglobulin (IgG, 2mg) and bovine serum albumin (BSA) were purchased from Sigma-Aldrich; glutaraldehyde was procured from SRL Chemicals; and antigen goat anti-mouse IgG serum solution (2mg, serum raised against mouse IgG) was obtained from Abcam. Indium Tin Oxide (ITO) coated glass was obtained from Macwin India.

2.2. Materials used

2.2.1 Synthesis of MOF: UiO-66

For the synthesis of UiO-66 the precursors used were metal salt zirconium chloride anhydrous ($ZrCl_4$ 98.0 % pure, Merck Life Science Pvt. Ltd), organic linker 1,4-benzene dicarboxylic acid (BDC, 98%, Sigma Aldrich®) and solvent used was n-dimethylformamide (DMF, 99% pure, Merck Life Science Pvt. Ltd) for synthesis and methanol (CH_3OH, 99.8% pure, Merck Life Science Pvt. Ltd) used for washing. The MOF UiO-66 was synthesized via a solvothermal route by mixing unimolar $ZrCl_4$ (1.1652 g), BDC (0.8306 g), and 1mL HCl (38% pure, Alfa Aesar®.) in 60 mL DMF. Later, 5 mg Benzoic acid (99.5% pure, Sigma Aldrich®) was also used as the modulator to slow down
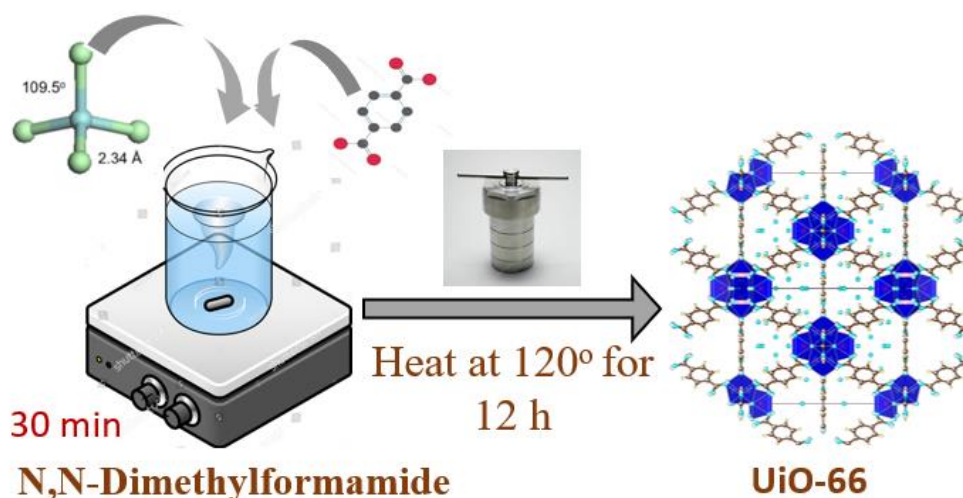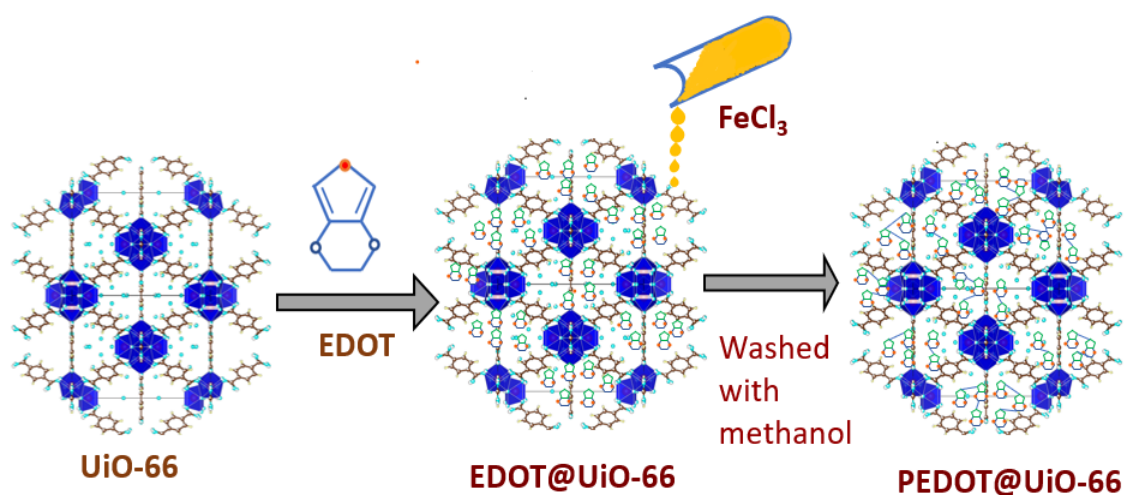
Fig. 2.1 Schematic of synthesis route of UiO-66.

the crystallization process in UiO-66 synthesis. After stirring the solution with a magnetic stirrer for 30 min, the mixture was oven heated in a teflon-lined stainless-steel autoclave at a temperature of 120 °C, for 12 h. The final product was obtained by centrifuging the processed solution and washing it several times with methanol and DMF followed by oven drying at a temperature of 100 °C, which yielded a white-coloured powder [25]. The synthesis route is shown in a scheme of Fig. 2.1.

2.2.2 In situ polymerization of PEDOT

First, 100 mg of pre-synthesized UiO-66 was exposed to 0.25 mL of 3,4-Ethylenedioxythiophene **(**EDOT, 97%, Alfa Aesar®**)** monomer and left undisturbed for 5 h in a glass vial at room temperature so that it gets soaked by the MOF. The EDOT adsorbed on the outer surface of the MOF was then washed with methanol. An alcoholic solution of ferric chloride **(**$FeCl_3$, 97 % pure, Sigma Aldrich®**)** has been added to the EDOT-loaded MOF and was kept under magnetic stirring (300 rpm) for about 12 h. The product was washed with methanol and deionized (DI) water for removing excess $FeCl_3$ till its colour turned white from yellow. The composite product was derived after drying in an oven at a temperature of 100 °C [26]. The synthesis route is shown in a scheme of Fig. 2.2.

Fig. 2.2 Schematic of synthesis route of PEDOT@UiO-66.

2.2.3 Synthesis of PEDOT

Firstly, 20 mL aqueous solution of $FeCl_3$ and 5.0 mL EDOT alcoholic solution were stirred in a magnetic stirrer separately in two different beakers, for about half an hour. The EDOT alcoholic sol was then added to the $FeCl_3$ solution under vigorous stirring as a result of which the colour turned black from orange after the two solutions got mixed. On subjected to stirring for 24 h, the precipitate is obtained by filtering and washing it with ethanol and DI water. Consequently, a dark blue coloured PEDOT powder is yielded after oven-drying at a temperature of 60 °C, for 24 h [27].

2.2.4 Synthesis of Ag_2O nanoparticles (NPs)

 For preparing Ag_2O nanoparticles, a 0.6 mM silver nitrate ($AgNO_3$, 99.9%, Sisco Research Laboratories Pvt. Ltd. (SRL) ^{O}) solution and a 0.5 mM sodium hydroxide (NaOH, 98%, Sisco Research Laboratories Pvt. Ltd. (SRL)) solution were prepared in two separate beakers. The $AgNO_3$ solution was stirred (990 rpm) for 2 hours at room temperature. The aqueous NaOH was added drop by drop into the mixture using a burette. The colour of the solution apparently turns brown from white, indicating the formation of Ag_2O nanoparticles. The mixture was ultrasonicated for 30 min and centrifuged (RPM@800) five times with deionized (DI) water. The resultant precipitate was filtered and dried in an oven for an hour at a temperature of 100 °C to yield the product Ag_2O NPs. [28]. The synthesis route is shown in a scheme of Fig. 2.3.
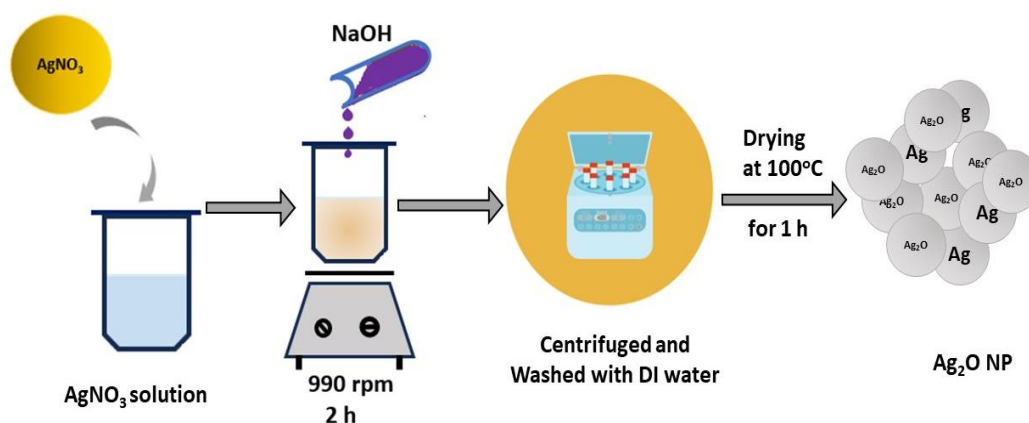
Fig. 2.3 Schematic of synthesis route of silver oxide nanoparticle (Ag$_2$O NP).

2.2.5   Synthesis of Ag$_2$O infiltrated UiO-66 MOF (S1(MOF))

Incorporation of Ag$_2$O in UiO-66, was considered by way of post synthetic modification method. Here, as-prepared UiO-66 (50 mg) was added to 8 mL acetonitrile with 30 mg AgNO$_3$. The mixture was then stirred for 4 h at room temperature. After the Ag$_2$O get imbued into UiO-66 the suspension was washed with acetonitrile by centrifugation to separate the solid composite from the solvent. The collected samples were taken into crucible for annealing at a temperature of 130^0C for 2 h in hot air oven to obtain the desired product of Ag$_2$O@UiO-66 composite, named as S1(MOF) [29]. The synthesis route is shown in a scheme of Fig. 2.4.
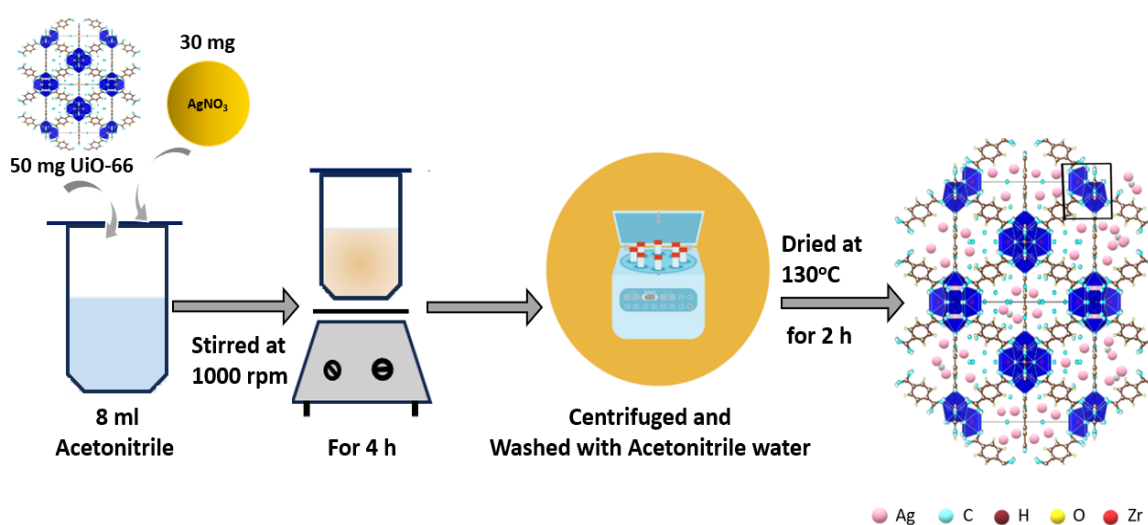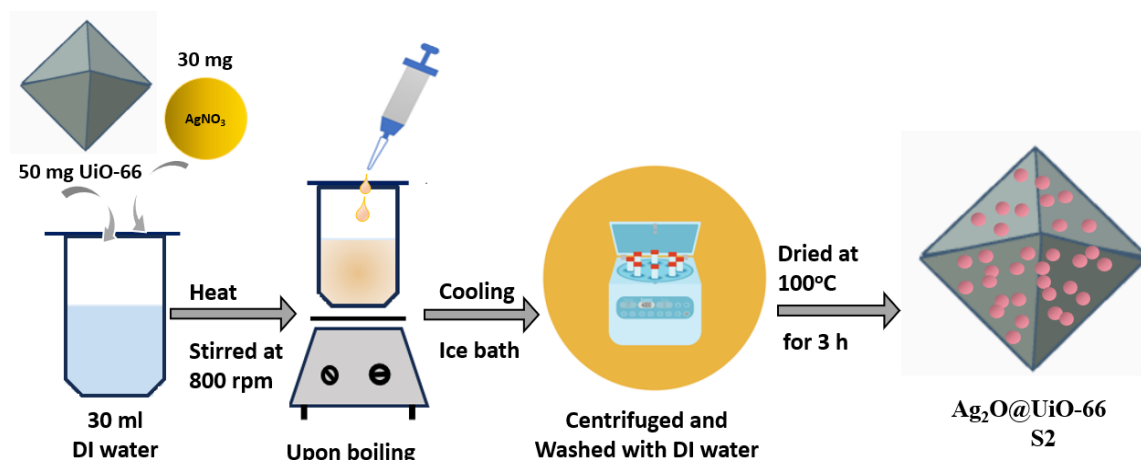

Fig. 2.4 Schematic of synthesis route of silver oxide nanoparticle (Ag$_2$O NP) infiltrated UiO-66 named as S1(MOF).

2.2.6   Synthesis of Ag₂O anchored UiO-66 MOF (S2(MOF))

Fig. 2.5 Schematic of synthesis route of silver oxide nanoparticle (Ag$_2$O NP) anchored UiO-66 named as S2(MOF).

A green synthesis route has been employed for obtaining Ag$_2$O NP decorated UiO-66. In this case, the reducing agent used for AgNO$_3$ reduction was an extract obtained from the banana root bulb (BRB) as reported in a recent work [30]. The BRB was cut into small pieces and washed thoroughly to remove all the soil and other dirt present in it. The small pieces were heated in DI water at a temperature of 100°C until it gets boiled. The extract was collected by filtering with Whatman® paper and stored at a temperature of 4°C for further use. Next Ag$_2$O@UiO-66-S2, 50 mg UiO-66 powder and 30 mg AgNO$_3$ were added in a 30 mL of DI water and allowed it to heat under stirring (RPM@800) until the solution boils. Once the solution started boiling, the BRB extract was added to the solution dropwise. On adding BRB extract the color of the solution is suddenly changed from white to light brownish, being the indicative of the desired reduction of Ag. The solution was then allowed to cool in an ice bath for further washing and adequate cleaning. A brown powder is obtained after annealing the sample at a temperature of 100° C in an oven. The composite of Ag$_2$O and UiO-66 received through this process was marked as, S2(MOF). The synthesis route is shown in a scheme of Fig. 2.5.

2.3 Fabrication of working electrodes

2.3.1 S1(MOF)/S2(MOF) on ITO coated glass

ITO coated glasses were used as the current collector substrate for the active layer of S1(MOF)/S2(MOF) in the role of working electrode for electrochemical sensing. Prior to modification, the large area ITO coated glasses were cut into 1 x 1.5 cm sized pieces and were subjected to washing with acetone ultrasonically. The electrode ink was prepared by mixing S1(MOF)/S2(MOF) powder sample, binder Nafion$^®$ (D-521 dispersion, 5% w/w in water and 1-propanol, Alfa Aesar®) and a conductivity enhancer carbon black in ethanol in a ratio of 75:10:5 which was further treated in an ultrasonic bath for homogeneous dispersion. The 10 µL electrode ink was drop-casted on the ITO pieces with the help of a micropippette and then dried in ambient environment (300 K).

2.3.2 PEDOT@UiO-66 on ITO coated glass

At first ITO coated glass was cut into pieces of dimension 1 x 1 cm and then cleaned it with acetone ultrasonically. A slurry of PEDOT@UiO-66 was prepared to modify the ITO surface by mixing it with 5w/w% PVDF as binder and 50 µL NMP as solvent using a mortar and pestle. The slurry was coated into the surface using a brush and allowed to dry at a temperature of 60º C. The prepared electrodes were than stored in the desiccator.

2.3.3 UiO-66 MOF fabricated on ITO coated glass for SHI irradiation experiment

The UiO-66 powder was fabricated into a film on ITO glass using a slurry coating technique in order to analyse the structural, morphological, and electrochemical performances after irradiation. Before fabrication ITO glass was cut into small pieces of 1 x 1.5 cm dimensions and washed in ethanol under ultrasonic cleaner. The slurry of active material was prepared by mixing 20 mg UiO-66 in 50 µL N-methyl 2- pyrrolidone (NMP) with the help of mortar and pestle. The slurry was deposited into ITO glass by a flat brush of size 2 mm to make a film of UiO-66 and allowed it to dry at 60º C. The UiO-66 films and were irradiated with SHI at Inter University Accelerator Centre (IUAC), New Delhi, India, using material science beam line. The films were irradiated with high energy (60

MeV) ions of N^{5+} with fluences of 5 x 10^{10}, 1 x 10^{11}, 5 x 10^{11}, 1 x 10^{12} ions/cm^2 under a vacuum of 10^{-6} torr projected in perpendicular direction.

2.3.4 Fabrication of pristine and irradiated UiO-66 with biomolecules

The immobilization of antibody mouse IgG on the pristine and irradiated UiO-66 films fabricated in ITO coated glass was carried out through cross-linking with glutaraldehyde (Gu). The as prepared UiO-66 films were first soaked in 2% (w/v) of Gu solution for 1 h and then rinsed with 50 mM PBS solution to remove the excess Gu from the electrode. The electrode was further incubated with 250 ng mL^{-1} mouse IgG for 1 h. The cross-linking between UiO-66 and mouse IgG is facilitated by Gu via binding to the hydroxyl group of UiO-66 and covalently binding with the amino acid of the antibody. The film was washed with PBS again to remove the unbounded mouse IgG. The final step includes the addition of a 2 mg/mL solution of bovine serum albumin (BSA) to block the non-specific open sites. After rinsed with PBS the IgG immobilized UiO-66 electrodes were stored at 4° C for further use.

2.4 Preparation of the analyte solution for electrochemical sensing

2.4.1 Preparation of Cd^{2+} and Hg^{2+} solution

Cadmium chloride (CdCl$_2$, 99.9% pure, Sigma Aldrich) stock solution of 0.1 mM was prepared by adding 1.83 mg CdCl$_2$ to 100 mL of DI water. 500 µL stock solution was diluted to a concentration of 1µM by adding 50 mL DI water for further use. Similarly, 0.1 µM concentration was prepared by adding 50 µL stock solution into 50 mL DI water. As for Hg^{2+} stock solution 2.71 mg Mercury chloride (HgCl$_2$, 99.5% pure, Sigma Aldrich) was mixed in 100 mL DI water and stirred for 3 h for homogeneous mixing. Again, the concentration of 1 µM Hg^{2+} solution was prepared by adding 50 mL DI water in 500 µL of the 0.1mM stock solution. Further the solution was diluted to 0.1 µM by adding 50 µL stock solution into 50 mL DI water.

2.4.2 Preparation of Catechol (CT) and hydroquinone (HQ) solutions

A 1mM stock solution was prepared by mixing 5.5 mg of catechol (CT, 99% pure, Alfa Aesar) and hydroquinone (HQ, 99% pure, alfa Aesar) in 50 ml DI water in separate vials.

To further prepare the three different concentrations of 100 µM, 10 µM, and 1 µM, 1 mL, 0.1 mL, and 0.01 mL of stock solution were added to 10 mL of DI water for each. During the quantitative sensing of analytes, the concentration of CT and HQ was varied from 1 µM to 320 µM. In order to obtain 1 µM analyte concentration 200 µL of 10 µM solution was added to 2 mL of supporting electrolyte tris buffer saline (TBS). Subsequently, the concentration was increased by adding different amount of 100 µM solution to 1 µM HQ/CT solution in TBS.

2.5 Characterization techniques

2.5.1 Powder X-ray Diffraction

X-ray diffraction (XRD) is a non-invasive analytical technique to determine the crystalline structure and explore the crystalline phase of a material under study. The diffraction pattern of X-rays can provide detailing as regards structural parameters like lattice constants, d-spacing, average crystallite size, diffraction planes, defects, crystal structure as well as % of crystallinity of the material etc. When monochromatic X-rays are dispersed at particular angles from a set of lattice planes in the sample, they constructively interfere to create XRD peaks. The source of the electrons produced in an X-ray tube is the tungsten filament. The electrons get released through thermionic emission when supplied with a voltage of approximately 40 kV. The electrons are directed towards the metal anode in the influence of high voltage across the electrodes. When a metal anode, such as copper, is exposed to an electron bombardment, the electrons in its first orbit are ejected. This causes the electrons in the second orbit to jump to the empty space and release energy in the form of X-rays. After being filtered to produce monochromatic radiation, the X-rays are collimated and directed at the sample. When the sample is illuminated with X-rays, they interact with the electron cloud surrounding the atom and scatters in all direction and interfere constructively as well as destructively. These waves cancel each other out destructively through interference in most directions, but according to Bragg's law, they add constructively in a few particular directions [31]-

$$2d \sin \theta = n\lambda \qquad (2.1)$$

Where d is the spacing between two crystal planes, θ is the incident angle of X-rays, λ is the wavelength of X-rays and n is the integer. During experimentation, the diffracted patterns resulting from the interaction of X-rays with the crystal lattice are captured by a detector. This detector records the intensity of the diffracted X-rays at various angles, forming a diffraction pattern. The collected data is then processed to convert the intensity measurements into a count rate, which represents the number of X-rays detected per unit time. The processed diffraction data, in the form of count rates, is typically output to a device such as a monitor for visualization and analysis.

XRD measurements for this research work were carried out with a Bruker AXS D8 Advance Powder X-ray diffractometer (with CuK_α radiation of wavelength $\lambda = 1.5406$ Å) operated at an accelerating voltage of 40 kV and current of 40 mA. The measurements were conducted with Bragg's diffraction angle, 2θ in range of 5° -60° and data acquisition in steps of 1°/min.

2.5.2 Fourier Transformed Infrared Spectroscopy

Fourier Transform Infrared Spectroscopy (FT-IR) is an analytical tool to determine different chemical bonds, function groups and molecular structure present in the given material. Infrared (IR) spectroscopy is the study on the interaction of infrared light with matter. Infrared light has a wavenumber range of 12,800 to 10 cm^{-1}. Typically, there are three regions in the IR spectrum - Far-IR is defined as radiation between 500 and 20 cm^{-1}, mid-IR between 4,000 and 500 cm^{-1} and NIR as typically between $\sim 10,000$ and 4,000 cm^{-1} [32]. When a material is illuminated with IR radiation it absorbs light at some specific frequencies depending on the type of bonds present in the molecule or type of atom present at the end of the bond. Upon IR absorption molecules get excited to higher vibrational or rotational level within the same electronic band. The IR absorption takes place only when there is a spontaneous change in dipole moment that would occur in the molecular system. It is widely accepted that these covalent bonds between atoms act as stiff springs with the ability to stretch, bend, twist, and scissor upon irradiation. When energy is absorbed by the molecule the fundamental excitations occur at the mid-IR region while overtones are occurred in the region of NIR region. In FTIR, the interferometer, detector, and source constitute the core components essential for analysing the interaction between matter and

infrared radiation. The source emits the infrared radiation used to probe the sample, with common sources including globar lamps or lasers depending on the experiment's requirements. The interferometer generates an interferogram by splitting infrared light into two beams, one interacting with the sample and the other serving as a reference, resulting in a signal containing information about the sample's absorption of specific infrared frequencies. The detector captures this interferogram and converts it into an electrical signal, which is then processed and digitized for further analysis. Together, these components enable FTIR spectroscopy to provide valuable insights into the chemical composition, structure, and functional groups present in the sample. Infrared radiation interaction results are represented in terms of transmittance (T) and wave numbers (in cm^{-1}). T is a measure of the radiant power transmitted through a sample relative to the incident radiation. It can also be expressed in terms of absorbance (A), which is the logarithm of the reciprocal of transmittance. Essentially, absorbance (A) is calculated by taking the negative logarithm of transmittance, providing a convenient way to quantify the extent of absorption by the sample. This relationship between transmittance and absorbance allows researchers to analyse how much of the incident infrared radiation is absorbed by the sample across different wavelengths, providing valuable insights into the sample's chemical composition and molecular structure [33].

Here in this research work IR active vibrational modes were recorded on an IMPACT 410 FTIR NICOLET spectrometer considering wavenumber range, 400-4500 cm^{-1}.

2.5.3 Raman spectroscopy

Raman spectroscopy is another non-invasive technique to identify the vibrational motions of the atoms present in a material. It differs from IR spectroscopy in a way that Raman active modes arises only when there is change in polarizability in the molecule under study. The underlying principle involves the inelastic scattering of monochromatic light by matter. Photons in monochromatic light undergo frequency alterations by virtue of inelastic scattering when impinge on the sample. In this technique the spectrometer receives the scattered light from the material and examine the molecular bonds present in the sample [34]. If the scattered light has same frequency as the incident one the scattering

is elastic and called as Rayleigh scattering. In Raman scattering the molecule absorbs a photon and electrons get excited to a higher energy level from the ground state. When the excited state transformed back to the ground state stimulated emission of photons takes place. The modes are referred to as Stokes lines if the scattered photon's energy is less than the incident photon, and Anti-Stokes lines if the energy is greater than the incident photon. Stokes lines are very weak in comparison with Rayleigh line as out of 10^7 of incident photons only about 1 photon scatters inelastically. Due to the scattering from an excited state and the relatively small number of atoms in an excited state, Anti-stokes lines are weaker.

Raman spectra for all the samples in this work were captured on a Renishaw spectrometer (Wotton-under-Edge, UK) employing a 514 nm laser, and data acquired in the range of 250-2000 cm^{-1}.

2.5.4 Scanning Electron Microscopy

Scanning electron microscopy (SEM) is a widely used versatile tool for obtaining information as regards morphology, topology, compositional differences, crystal orientation, presence of defects etc. It uses energetic electrons to scan the specimen surface and backscattered or secondary electrons to create the image eventually. The source electrons are produced via thermionic emission from a tungsten filament or, lanthanum hexaboride (LaBO$_6$) cathode. In the case of a tungsten filament, electrons are emitted when the filament is heated to a high temperature, causing thermionic emission. Similarly, in a LaB$_6$ cathode, electrons are emitted from the surface of the cathode material under high temperature conditions. The generated electrons are accelerated through an electric potential ranging from 0.2 to 40 kV, depending on the desired energy for the specific electron microscopy application. An optical column plays a crucial role in ensuring that the incoming electrons have consistent energy and trajectory. The optical column consists of a series of electromagnetic lenses and apertures that manipulate and focus the electron beam emitted from the electron source. By adjusting the magnetic fields generated by these lenses, the electron beam is precisely directed onto the sample surface, ensuring that it follows a specific path and scans the surface in a controlled manner. Both elastic and inelastic interactions occur between the specimen's atoms and the electron beam. When electrons interact with the nuclei of atoms and elastically scatter at large angles ranging

from 0° to 180°, they are referred to as backscattered electrons (BSEs). The intensity of backscattered electrons is influenced by the atomic number of the material being examined. Materials with higher atomic numbers tend to produce more intense backscattered electron signals due to stronger elastic scattering interactions between the incident electrons and the nuclei of the atoms in the specimen [35]. The distribution of different elements in a material can be obtained from the images produced from backscattered electrons (BSE) in scanning electron microscopy (SEM). Backscattered electrons are sensitive to variations in atomic number within the sample. Since the intensity of backscattered electrons is influenced by the atomic number of the material, regions with higher atomic numbers appear brighter in BSE images, while regions with lower atomic numbers appear darker. By analysing the contrast differences in BSE images, researchers can infer the distribution of different elements within the sample. When high-energy electrons from the electron beam interact with a specimen, loosely bound electrons can be scattered from the surface. These scattered electrons are termed as secondary electrons (SE). Unlike backscattered electrons, secondary electrons originate from the outermost layers of the specimen, typically within a depth of 5-50 nanometres from the surface. Due to their shallow origin, secondary electrons provide valuable information about the surface morphology and topography of the specimen. By detecting and collecting these secondary electrons, SEM can generate high-resolution images that reveal fine surface details such as texture, roughness, and surface features. To collect both SE and BSE signals in SEM, a positive voltage is applied to the collector located in front of the detector. This positive voltage serves to attract the negatively charged electrons emitted from the specimen surface towards the detector. A photomultiplier device is used to amplify the electrical signals of the collected electrons. Once the signals have been amplified by the PMT, they are typically supplied to a cathode-ray tube (CRT) for image display. The CRT converts the amplified signals into a visual representation on a screen, allowing the SEM operator to observe the surface morphology and topography of the specimen in real-time [36]. Apart from this Auger electrons and X-rays are also generate during scattering. Auger electrons are low- energy electrons emitted from atoms when an inner-shell electron is ejected and replaced by an outer-shell electron. This process occurs when high-energy electrons from the electron beam collide with atoms in the specimen, causing the ejection of an inner-shell electron. The resulting electron vacancy is filled by an outer-shell electron, releasing energy in the form of an Auger electron. By measuring the wavelength of these X-rays

elemental composition of the material can be determined. This method is known as energy dispersive X-ray spectroscopy (EDX). With advanced technology SEM has been upgraded to FESEM where electrons are generated by a field emission gun. The image formed by FESEM are cleaner with better resolution and fewer electrostatic distortion due to the narrow and focused beam.

SEM images and EDX measurements were acquired on a scanning electron microscope of model JEOL JSM 6390 LV with a 20 kV accelerating voltage at Tezpur University. Field emission scanning electron microscope (FE-SEM) images were captured from ZEISS Sigma 300 installed in Gauhati University.

2.5.5   High resolution transmission electron microscopy

High resolution transmission electron microscopy (HRTEM) uses transmitted electrons to characterize nanostructured materials. It can give information about the internal microstructure of the material up to 0.1 nm resolution. In TEM a beam of electrons is allowed to transmit through an ultra-thin specimen, and the information provided by the interactions of the electrons with the specimen reveals the details about its composition, crystal structure, and morphology. The process is carried out under vacuum where the electron source is tungsten filament or, $LaBO_6$ behaving as the cathode. On applying a high voltage of 40 to 400 kV to the anode, a stream of electrons accelerates towards the anode, which is focused with the help of electrostatic and electromagnetic lenses to pass through the specimen. As the electron beam passes through the specimen, it interacts with the atoms and electrons in the material, undergoing scattering, diffraction, and absorption processes. The transmitted electron beam from the specimen is collected on imaging devices like photographic film or fluorescent screen or detectors such as CCD camera. The collected electron beams are magnified and focused by the objective lenses of the microscope before it collected for imaging. The processed image is then projected in the monitor of the computer. The degree of resolution of the images are determined by the objective lenses while the magnification of the images is achieved through the combination of the objective lenses and the imaging plane. The imaging plane, also known as the projection lens or projector system, is responsible for projecting the magnified image of the specimen onto a screen or detector [37]. The wavelength and energy of the radiation also plays the role in enhancing the resolution and magnification. Apart from imaging diffraction pattern which

determines the crystallinity of the material can be obtained by focusing the electron beam at small portion of the specimen, the technique is known as Selected Area Electron Diffraction (SAED). In SAED, a selected area of the specimen is illuminated with a highly focused electron beam. The electrons interact with the crystal lattice of the specimen, resulting in diffraction patterns that are characteristic of the crystalline structure of the material within the illuminated area. These diffraction patterns consist of a series of bright spots or rings, which correspond to the specific arrangement of atoms within the crystal lattice. By analyzing the positions and intensities of the spots or rings in the diffraction pattern, valuable information about the crystal structure, orientation, and degree of crystallinity of the material can be obtained.

The TEM imaging has been performed in transmission electron microscope installed at Sophisticated Analytical Instrumentation Centre (SAIC) at Tezpur University, India. The model is TECNAI G2 20 S-TWIN (200KV) (FEI COMPANY, USA) with resolution 2.4 Å and the accelerating voltage was 200 kV. The sample preparation for imaging was carried out by dispersing 1 mg sample in 2 mL ethanol followed by sonication. Then the solution was drop casted on carbon coated copper grid for imaging.

2.5.6 N_2 adsorption-desorption measurements

To determine the porous structure of a material low-pressure nitrogen (N_2) adsorption-desorption isotherm is carried out at 77.3 K. At low temperatures nitrogen molecules are adsorbed onto the surface of the material, particularly within its pores and voids. The adsorption process is characterized by the amount of nitrogen gas adsorbed as a function of pressure, resulting in an adsorption isotherm. Prior to the adsorption-desorption process the chamber is evacuated at 120-200º C followed by cooling it to liquid nitrogen (LN_2) temperature. In the adsorption branch the pressure on the N_2 is increased gradually to saturated pressure (P_o) and in the desorption process step-wise reduction of pressure would take place until it attains the initial value. The nitrogen gas adsorbed and desorbed at every equilibrium pressure and temperature are noted. To analyse these data, volume of nitrogen gas adsorbed and desorbed are plotted against the relative pressure i.e. P/P_o. The most common way to characterise porous materials is using pore sizes that are obtained from the gas sorption data. To represent the link between porosity and sorption events, IUPAC conventions have been established to categorise pore sizes and gas sorption isotherms.

This method is widely used to evaluate the specific surface area of the material by fitting the data points to Brunauer-Emmet-Teller (BET) equation. Porosity can also be analysed from this physisorption method with the help of models like Barrett–Joyner–Halenda (BJH), Dollimore and Heal (D-H), Horvath–Kawazoe (HK), and the density functional theory (DFT) models [38].

At a liquid nitrogen temperature of 77 K, nitrogen adsorption-desorption measurements were performed using the Quantachrome (NOVA 1000E) analyser. The BET method was employed to quantify the samples' specific surface areas based on the adsorption data, and the H-K method was used to determine the pore volume and pore size distribution based on the desorption data.

### 2.5.7 Current-voltage (I-V) characteristics

The change in current on applying a linear sweep voltage gives the current-voltage characteristics of a specimen of interest. When DC voltage is applied the measured current is DC. The electrical properties are determined from the pattern of the I-V curve. Parameters like resistivity, conductivity etc. are analysed from the I-V data. On applying various models transport property of the charge carrier present in the specimen can be evaluate at large. The most commonly used method is two probe method which involves making two contacts on the sample surface using thin lead wires, and measuring the current flow across the sample's two ends by adjusting the voltage. Another method is four probes where four probes are evenly spaced around 1 mm apart in a straight line. Voltage is monitored across the inner two probes while current is applied between the outer two probes.

The DC conductivity measurements were performed with a two-probe setup connected to a Keithley 2400 source meter® in a voltage range of -10 V to 10 V in electrodes. The temperature dependent characteristics were measured by placing the sample connected with two probes in brass chamber with voltage regulator to maintain the temperature.

2.6 Evaluation of electrochemical properties

2.6.1 Cyclic Voltammetry (CV)

Cyclic voltammetry is an electrochemical technique used to evaluate the current response of a redox active solution to a linearly cycled potential sweep between two or more predefined values. The CV allows to extract many information about the electrode material such as capacitance, conductivity, reversibility of the redox reaction, position of the redox peaks, thermodynamics of the reactions, mass transport and adsorption mechanisms etc. [39]. As for CV measurement a potential of triangular waveform is normally applied across the working electrode and the current response is recorded at large. The potential at the working electrode starts from a particular value say E1 and scans for a certain time to attain final potential E_2. The scan is then reverse to the initial potential E_1 to complete the cyclic voltammogram (Fig. 2.6 (a)). The rate at which potential was scanned is known as scan-rate which is kept constant during the cycle. When the potential is scanned anodically from point A to C via path B (Fig. 6 (b)) the analytes present in the electrolyte near the working electrode oxidizes. At point B anodic peak current (I_{pa}) is observed where current is more due to the diffusion of additional analytes from the bulk solution. The production of a large number of oxidized analytes causes a depletion layer to form at the electrode and electrolyte interface. Thus, on further increase in the positive potential will reduce the rate of diffusion of analytes from the bulk solution, resulting in reduction in the current as the potential scans from B to C. At point C the potential is reversed to scan in negative direction. The oxidized analytes near the electrode surface now starts to reduce under the influence of negative potential. The current decreases until it reaches redox potential at which overall reduction of analytes takes place resulting into cathodic current (I_{pc}) giving rise to the reduction peak at point D. The parameters like I_{pc} and I_{pa}, separation of redox peaks E_{pa} and E_{pc} (ΔE_p) etc. can be obtained from the voltammograms. These characteristics are extremely helpful in comprehending the electron transfer process at the electrode-electrolyte interface during an electrochemical reaction. If the peak-to-peak separation (ΔE_p) is 57 mV at 25° C and the width at half max on the oxidation peak is 59 mV the reaction is electrochemically reversible. In the reversible process the electron transfer kinetics between electrode and analyte is fast and it obeys the Nernst equation. When the value of ΔE_p deviates from the required condition the reaction could be quasi-reversible or irreversible [40].
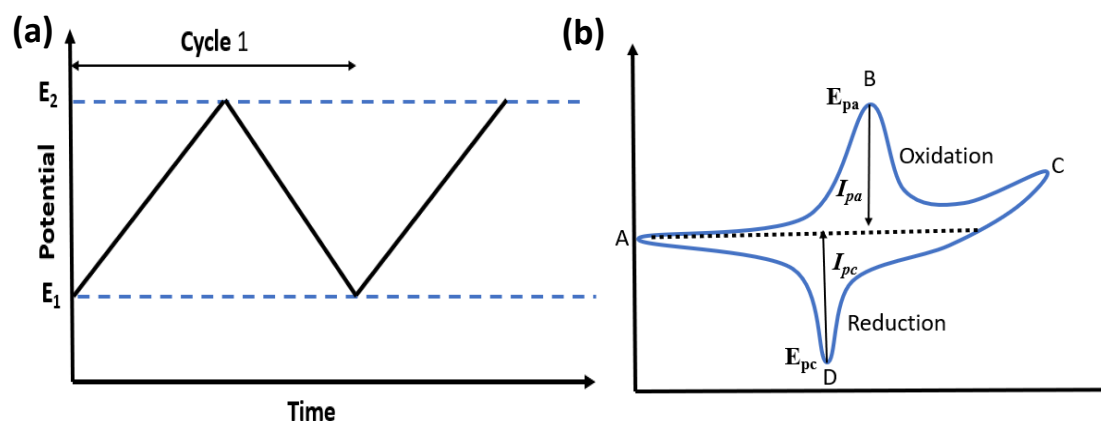
Fig. 2.6 (a) Triangular potential waveform used in cyclic voltammetry showing the variation of potential from an initial value (E1) to a final value (E2).

The CV measurements were recorded on a Gamry interface 1010 E potentiostat in a three-electrode system with Ag/AgCl as a reference electrode and platinum as counter electrode. The electrolytes used at different stages were potassium chloride (KCL), phosphate buffer saline (PBS), tris buffer saline (TBS), ferry-ferro cyanide Fe $[(CN)_6]^{3-/4}$ etc.

2.6.2 Electrochemical Impedance Spectroscopy (EIS)

Electrochemical impedance spectroscopy (EIS) is an important electrochemical technique for examining various chemical, electrochemical, and surface processes occurring at the interface between the electrode and electrolyte. An alternative potential of small amplitude is applied with varying frequency is applied across the electrodes and the current is measured to obtain the frequency dependent resistances occurring at different part of the electrochemical setup. Through EIS many complex non-ohmic processes taking place at the interface of electrode and electrolyte can be determined with good precision and reliability [41]. These processes arise because of the obstacle faced by the charge carriers due to various electrochemical phenomena occurring at the interface like formation of double layer capacitance, migration of charge carriers from the bulk of the solution to the electrode surface, hindrance in flow of co-ions and counter ions due the presence of multiple species in the solution etc (Fig.7(a)). In the electrochemical reaction faradic current due to transfer of electrons between electroactive material is accompanied by a non-faradic current or capacitive current. That non-faradic component is due to the accumulation of charged particles near the electrode giving rise to a capacitive layer. When

an AC potential ($E_t = E_o \sin(\omega t)$) is applied to the experimental setup both faradic and non-faradic current ($I_t = I_o \sin(\omega t + \varphi)$) faces a complex resistance that is called impedance(Z) given by-

$$Z = \frac{E_o \sin(\omega t)}{I_o \sin(\omega t + \varphi)} = Z_0 \frac{\sin \omega t}{\sin(\omega t + \varphi)} \tag{2.2}$$

Here, Z is the frequency dependent impedance which can be expressed in an equivalent circuit consist of resistors, capacitors and inductors (Fig.7 (b)). Total impedance $Z(\omega)$ has a real component Z' and an imaginary component Z''. Therefore, total impedance is given by-

$$Z(\omega) = Z' + j(-Z'') \quad \text{where } j = \sqrt{-1} \tag{2.3}$$

The real part of the impedance is the frequency independent resistance and the imaginary part appears due to the phase difference between current and voltage. If the phase difference is positive the reactance is inductive $X_L = \omega L$ and when the phase difference is negative the reactance is capacitive $\left(X_C = -\frac{1}{\omega C}\right)$ with L as the inductance and C as the capacitance. When the real vs. imaginary impedance is plotted, it results in Nyquist plot from which quantitative information about the different reactance can be extracted. The imaginary impedance (Y-axis) is negative while X-axis represents a positive real impedance at every point. Nyquist plot can be expressed as Randles equivalent circuit that consist of resistors, capacitors and inductors as shown in Fig. 2.7 (b) [42].

The total impedance from Randles circuit can be represent as-

$$Z(\omega) = R_s + \frac{R_{ct}}{1 + \omega^2 R_{ct}^2 C_{dl}^2} - j \frac{\omega R_{ct}^2 C_{dl}}{1 + \omega^2 R_{ct}^2 C_{dl}^2} \tag{2.4}$$

Where real part of the impedance is-

$$Z'(\omega) = R_s + \frac{R_{ct}}{1 + \omega^2 R_{ct}^2 C_{dl}^2} \tag{2.5}$$
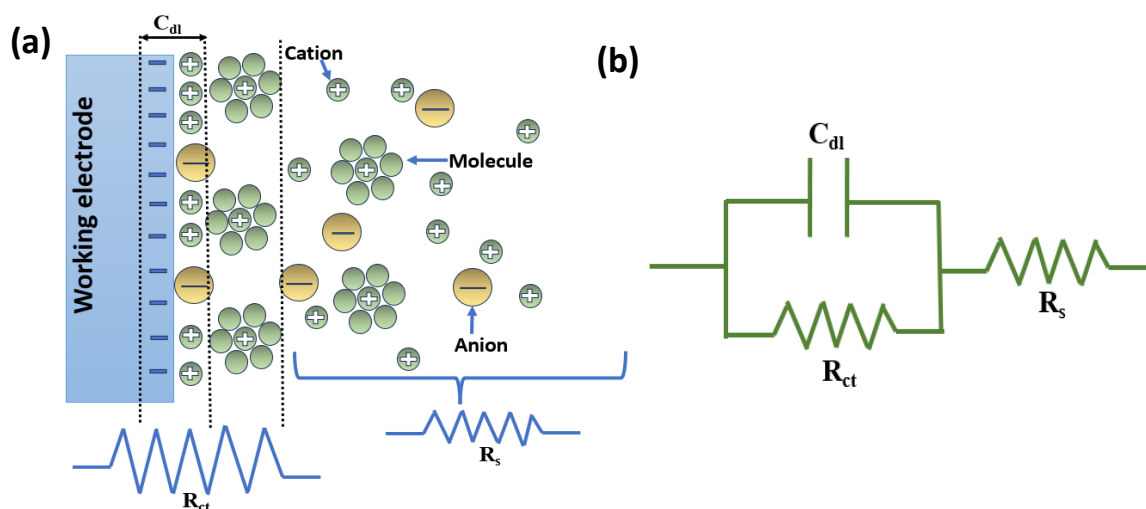
Fig. 2.7 (a) Schematic to describe the EIS circuit and the redox reaction that takes place at the surface of working electrodes in a conventional-electrochemical cell, (b) Randle's equivalent circuit containing the reactants.

And imaginary part is-

$$Z''(\omega) = -\frac{\omega R_{ct}^2 C_{dl}}{1+\omega^2 R_{ct}^2 C_{dl}^2} \tag{2.6}$$

At higher frequency i.e the part of X-axis near to origin represents the solution resistance R_s as $\omega \to \infty$. At a lower frequency equation (2.5) becomes $Z'(\omega) = R_s + R_{ct}$ as $\omega \to 0$. Therefore, Nyquist plot comprises a semicircle whose diameter is the indicative value of charge transfer resistance (R_{ct}). On the other hand, the imaginary impedance $Z''(\omega)$ becomes highest when frequency becomes maximum (ω_{max}) which can be written as [43] -

$$\omega_{max} R_{ct} C_{dl} = 1 \tag{2.7}$$

Where, $$C_{dl} = \frac{1}{\omega_{max} R_{ct}} \tag{2.8}$$

The EIS measurements for the prepared electrodes with as synthesized materials were obtained from Metrohm Autolab model ECI10® and Gamry interface 1010E electrochemical work stations in three probe setups.

2.6.3 Differential pulse voltammetry (DPV)

Voltammetry is the term used to represent to all current-voltage techniques that apply varying potential to the working electrode with respect to a reference electrode and measure the resulting current at the potential for oxidation or reduction of the analyte. In DPV the potential is applied in the form of pulse for 50-60 milliseconds. Pulse is introduced to increase the sensitivity by improving the ratio of Faradic to capacitive current. In DPV the applied potential is a series square-wave pulse of constant amplitude superimposed with a slowly changing DC potential sweep [44]. This method differs from the normal differential voltammetry in terms of the measuring current. Here the current is measured in two points for each pulse, first just before the pulse is started and second at the end of the pulse. The difference between the two currents is recorded and displayed with respect to the DC potential. The capacitive current rapidly increases and then decreases exponentially as the pulse ends. This rapid decay in capacitive current is due to the fast charging and discharging of the double layer, which occurs on a timescale governed by the characteristics of the electrode-electrolyte interface. As the pulse ends, the capacitive current rapidly returns to baseline levels. On the other hand, faradaic current, which is associated with electrochemical reactions, typically decays more slowly. The decay of faradaic current is often described by a function of $1/(time)^{1/2}$, indicating a slower decrease over time compared to the exponential decay of capacitive current. Therefore, the only the faradic current is obtained at the end of potential each pulse[45]. The resulting voltammograms are peaked shaped which varies with the concentration of the analyte.

This method is an electroanalytical technique used to detect and quantify the trace of electroactive analytes in a solution. Another technique used for same purpose is differential pulse stripping voltammetry (DPSV). DPSV combines aspects of both voltammetry and stripping analysis to achieve high sensitivity and selectivity. In DPSV, a potential waveform is applied to the working electrode in a series of discrete pulses, typically, with a small amplitude and a short duration. These pulses are superimposed onto

a linear potential ramp, allowing for the accumulation of the analyte species at the electrode surface during each pulse. Following each pulse, a differential pulse is applied to the electrode, causing the stripping of the accumulated species from the electrode surface. The resulting current response, measured as a function of the applied potential, provides information about the concentration of the analyte species in the solution.

The DPV and DPSV techniques were employed for qualitative and quantitative analysis of trace heavy metal ions, hydroxybenzene isomers and bio-analytes in electrolyte solution. The experiments were performed in electrochemical workstation Gamry interface 1010E® with three probe mode at step size of 5 mV.

2.7 Conclusion

In summary, we have discussed the general properties and source of the precursors used to obtain the desired product according to the objectives set. In addition, a thorough synopsis of the materials' synthesis process and the detailed experimental techniques have been included in this chapter. The MOF was obtained through a solvothermal method carried out at a temperature of 120º C. Moreover, the guest was loaded into the MOF through various post-synthetic routes. Electrode fabrication for further investigations, like SHI irradiation, electrochemical and sensing behaviour studies were also highlighted in this chapter. The experimental details presented herein outlined the precise methodologies employed to characterize the synthesized materials. Techniques such as X-ray diffraction, scanning electron microscopy, N_2 adsorption, FT-IR, Raman etc. were employed to analyse the structural, morphological, and compositional properties of the materials, the result of which are described vividly in Chapter 3. The electrical characteristics were performed via a two-probe *I-V* measurement setup on a Keithley® 2400 source meter, while electrochemical studies have been carried out at the potentiostat Gamry interface 1010E®. The results of these experiments have also been discussed in the subsequent chapters of the thesis.

References

[1]   Lee, Y. R., Kim, J. & Ahn, W. S. Synthesis of metal-organic frameworks: A mini review. *Korean Journal of Chemical Engineering*. **30**: 1667–1680, 2013.

[2]   Stock, N. & Biswas, S. Synthesis of metal-organic frameworks (MOFs): Routes to various MOF topologies, morphologies, and composites. *Chemical Reviews*. **112**: 933–969, 2012.

[3]   Safaei, M. *et al.* A review on metal-organic frameworks: Synthesis and applications. *TrAC - Trends in Analytical Chemistry*. **118** 401–425, 2019.

[4]   Zou, D., Liu, D. & Zhang, J. From Zeolitic Imidazolate Framework-8 to Metal-Organic Frameworks (MOFs): Representative Substance for the General Study of Pioneering MOF Applications. *Energy and Environmental Materials*. **1**: 209–220, 2018.

[5]   Shahrokhian, S., Khaki Sanati, E. & Hosseini, H. Direct growth of metal-organic frameworks thin film arrays on glassy carbon electrode based on rapid conversion step mediated by copper clusters and hydroxide nanotubes for fabrication of a high performance non-enzymatic glucose sensing platform. *Biosens Bioelectron.* **112**: 100–107 ,2018.

[6]   Wang, Z., Liu, H., Wang, S., Rao, Z. & Yang, Y. A luminescent Terbium-Succinate MOF thin film fabricated by electrodeposition for sensing of Cu2+ in aqueous environment. *Sens Actuators B Chem.* **220**: 779–787 ,2015.

[7]   Li, M. & Dincă, M. Reductive Electrosynthesis of Crystalline Metal–Organic Frameworks. *J Am Chem Soc.* **133**: 12926–12929 ,2011.

[8]   Beamish-Cook, J., Shankland, K., Murray, C. A. & Vaqueiro, P. Insights into the Mechanochemical Synthesis of MOF-74. *Cryst Growth Des.* **21**: 3047–3055 ,2021.

[9]   Chen, D., Zhao, J., Zhang, P. & Dai, S. Mechanochemical synthesis of metal–organic frameworks. *Polyhedron.* **162**: 59–64 ,2019.

[10] Qiu, S. & Zhu, G. Molecular engineering for synthesizing novel structures of metal–organic frameworks with multifunctional properties. *Coord Chem Rev.* **253**: 2891–2911 ,2009.

[11] Schaate, A. *et al.* Modulated synthesis of Zr-based metal-organic frameworks: From nano to single crystals. *Chemistry - A European Journal.* **17**: 6643–6651 ,2011.

[12] Zhang, J. *et al.* A polythiophene/UiO-66 composite coating for extraction of volatile organic compounds migrated from ion-exchange resins prior to their determination by gas chromatography. *J Chromatogr A.* **1633**: ,2020.

[13] Phan, P. T., Hong, J., Tran, N. & Le, T. H. The Properties of Microwave-Assisted Synthesis of Metal–Organic Frameworks and Their Applications. *Nanomaterials.* **13**: 352 ,2023.

[14] Beamish-Cook, J., Shankland, K., Murray, C. A. & Vaqueiro, P. Insights into the Mechanochemical Synthesis of MOF-74. *Cryst Growth Des.* **21**: 3047–3055 ,2021.

[15] Diah Rahmawati, I., Ediati, R. & Prasetyoko, D. *Synthesis of UiO-66 Using Solvothermal Method at High Temperature. Journal of Proceeding Series.* **1**, 2014.

[16] PubChem Compound Summary for CID 7489, T. acid. National Center for Biotechnology Information (2024). PubChem Compound Summary for CID 24817*, Zirconium tetrachloride.*

[17] National Center for Biotechnology Information (2024).PubChem Compound Summary for CID 313, *H. Acid*.

[18] PubChem Compound Summary for CID 702, Ethanol. National Center for Biotechnology Information (2024). PubChem Compound Summary for CID 6342*, Acetonitrile.*

[19] PubChem Compound Summary for CID 6228, N. N.-D. National Center for Biotechnology Information (2024). PubChem Compound Summary for CID 887*, Methanol.*

[20] Guo, Q. *et al.* Physical and Electrochemical Properties of Soluble 3,4-Ethylenedioxythiophene (EDOT)-Based Copolymers Synthesized via Direct (Hetero)Arylation Polymerization. *Front Chem* **9**: 753840 ,2021.

[21] PubChem Compound Summary for CID 24470, S. N. National Center for Biotechnology Information (2024), *Silver Nitrate*.

[22] National Center for Biotechnology Information (2024). PubChem Compound Summary for CID 24380, *Ferric Chloride*. PubChem Compound Summary for CID 14798, *Sodium Hydroxide.*

[23] Suresh, S., Srivastava, V. C. & Mishra, I. M. Adsorption of catechol, resorcinol, hydroquinone, and their derivatives: a review. *International Journal of Energy and Environmental Engineering.* **3**: 32 ,2012.

[24] Horn, J. D. Cadmium, Physical and Chemical Properties. in *Encyclopedia of Metalloproteins* 383–384 (Springer New York, New York, NY, 2013).

[25] Tan, Y., Zhang, W., Gao, Y., Wu, J. & Tang, B. Facile synthesis and supercapacitive properties of Zr-metal organic frameworks (UiO-66). *RSC Adv.* **5**: 17601–17605 ,2015.

[26] Le Ouay, B. *et al.* Nanostructuration of PEDOT in Porous Coordination Polymers for Tunable Porosity and Conductivity. *J Am Chem Soc.* **138**: 10088–10091 ,2016.

[27] Zhao, Q., Jamal, R., Zhang, L., Wang, M. & Abdiryim, T. The structure and properties of PEDOT synthesized by template-free solution method. *Nanoscale Res Lett.* **9**: 557 ,2014.

[28] Rajakumari, R., Priya, C. & Srilekha, A. Synthesis and Characterization of Nano Ag2O and Cu(OH)2 by Solution Reduction Method and Their Antibacterial Studies. *Journal of Nanoscience and Technology.* **4**: 435–438 ,2018.

[29]   Surya, S. G. *et al.* A silver nanoparticle-anchored UiO-66(Zr) metal-organic framework (MOF)-based capacitive H2S gas sensor. *CrystEngComm.* **21**: 7303–7312 ,2019.

[30]   Neog, A., Das, P. & Biswas, R. A novel green approach towards synthesis of silver nanoparticles and it's comparative analysis with conventional methods. *Applied Physics A.* **127**: 913 ,2021.

[31]   Sayeed, M. A. Electrochemical fabrication of nanostructured metal oxides for the oxygen evolution reaction. Queensland University of Technology, 2018.

[32]   Berthomieu, C. & Hienerwadel, R. Fourier transform infrared (FTIR) spectroscopy. *Photosynth Res.* **101**: 157–170 ,2009.

[33]   Banwell, C. N. and M. E. M. *A Book: Fundamentals of Molecular Spectroscopy.* McGraw Hill Education, 2002.

[34]   Vašková, H. A powerful tool for material identification: Raman spectroscopy. Int. J. Math. Model. Methods Appl. Sci, 5:1205-1212, 2011. *Int. J. Math. Model. Methods Appl. Sci.* **5**: 1205–1212 ,2011.

[35]   Preet, A. & Lin, T.-E. A Review: Scanning Electrochemical Microscopy (SECM) for Visualizing the Real-Time Local Catalytic Activity. *Catalysts.* **11**: 594 ,2021.

[36]   Polcari, D., Dauphin-Ducharme, P. & Mauzeroll, J. Scanning Electrochemical Microscopy: A Comprehensive Review of Experimental Parameters from 1989 to 2015. *Chem Rev.* **116**: 13234–13278 ,2016.

[37]   Kaufmann, E. N. *Characterization of Materials.* John Wiley & Sons, Inc., Hoboken, New Jersey, 2003.

[38]   Alothman, Z. A. A review: Fundamental aspects of silicate mesoporous materials. *Materials*. **5**: 2874–2902, 2012.

[39]   Nicholson, R. S. Theory and Application of Cyclic Voltammetry for Measurement of Electrode Reaction Kinetics. *Anal Chem.* **37**: 1351–1355 ,1965.

[40]   Elgrishi, N. *et al.* A Practical Beginner's Guide to Cyclic Voltammetry. *J Chem Educ.* **95**: 197–206 ,2018.

[41]   Y. Sulaiman. Sulaiman, Y., Characterisation of pedot and its derivatives in electrochemical sensing applications. Durham University, United Kingdom, 2012.

[42]   Magar, H. S., Hassan, R. Y. A. & Mulchandani, A. Electrochemical Impedance Spectroscopy (EIS): Principles, Construction, and Biosensing Applications. *Sensors.* **21**: 6578 ,2021.

[43]   Wang, S. *et al.* Electrochemical impedance spectroscopy. *Nature Reviews Methods Primers*. **1**: 41, 2021.

[44]   Shuman, L. M. *Differential Pulse Voltammetry. Methods of Soil Analysis. Part 3. Chemical Methods-SSSA Book Series* 1996.

[45]   Pulse voltammetric methods of analysis. *Philosophical Transactions of the Royal Society of London. Series A, Mathematical and Physical Sciences.* **302**: 315–326 ,1981.